AIAA JOURNAL
Vol. 50, No. 12, December 2012

Experimental and Numerical Investigation of a Wing-Body Junction Flow

Fabien Gand,* Vincent Brunet,† and Sébastien Deck‡
ONERA—The French Aerospace Lab, F-92190 Meudon, France

DOI: 10.2514/1.J051462

This article presents a study of a simplified wing-body junction. The main purpose of this work is to provide insights on the abilities of some industrial and research numerical approaches to accurately reproduce the flow for that type of configuration. To this end, a test case based on a NACA012 wing is designed at $Re_c = 2.8 \times 10^5$. An experimental database was created and used as validation data for the evaluation of Reynolds-averaged Navier–Stokes and large-eddy simulation computations. The sensitivities of the configuration to flow conditions such as the incoming boundary-layer thickness and the angle of attack are explored. The study points out the limitations of the Reynolds-averaged Navier–Stokes models investigated, which are highly sensitive to the grid density. Conversely, the large-eddy simulation is shown to be able to reproduce the experimentally observed flow features within the junction.

Nomenclature

c	=	wing chord
R_0	=	leading edge radius
Re_x	=	Reynolds number based on length x
S_T	=	distance from the leading edge along the airfoil surface to the maximum thickness
T	=	maximum thickness of the wing
X_T	=	chordwise position of T
y^+	=	wall viscous units
δ	=	boundary-layer thickness
θ	=	boundary-layer momentum thickness

I. Introduction

CORNER separations that can appear at wing-body junctions is a well-known issue in the fields of aircraft design, turbomachinery, and wind-tunnel experiments (in this case one may talk about side-wall effects). It appears that the development of two perpendicular boundary layers is likely to onset separation at the junction, which is prejudicial in terms of drag and total pressure losses, and it can even trigger wing stall.

A lot of authors have investigated the junction region, both experimentally and numerically. However, while applied aerodynamic configurations tend to show that the key separation appears at the bottom of the corner region [1], as depicted in Fig. 1, most of the studies have been focusing on the horseshoe vortex that appears when the upstream boundary layer of the body encounters the leading edge of the wing. On the numerical side, studies dealing with corner separations on technical configurations emphasize the effect of the grid on the simulations [2,3] and suffer from the lack of experimental databases to thoroughly validate the computational fluid dynamics (CFD) results. Detailed literature reviews [4,5] provide insights on the physics of junction flows and their characteristic parameters.

From the large amount of literature covering the topic of junction flows, one can extract basic flow parameters to describe the properties of a junction flow: the angle of attack, the incoming boundary-layer thickness (δ) and two scaling parameters of the horseshoe vortex: the bluntness factor (BF) [6] and the momentum deficit factor (MDF) [7]. The BF is characteristic of the aspect ratio of the nose of the wing, and the MDF is characteristic of the Reynolds number and the ratio of the boundary-layer thickness and wing thickness. Figure 2 illustrates the values of these parameters for the major junction flow studies found in the literature. It appears that there are very few studies investigating corner separations, which explains the lack of physical analysis for this phenomena. Using these diagrams, we can only conjecture some sets of flow conditions under which a junction flow may be likely to be dominated by a massive horseshoe vortex, or, conversely, by a corner separation. These conditions are highlighted in Fig. 2. Nevertheless, the data from the literature are too sparse to provide a physical explanation for this behavior.

As a conclusion, two issues are raised by the previous studies found in the literature. For industrial configurations, corner separation is among the most critical matters, but its underlying physics remain unclear. Furthermore, the numerical simulation of junction flows is challenging, but it is a major concern in the framework of the current increase in CFD-based aircraft design.

The present article addresses this second topic. The purpose is to assess various turbulence closures available in an industrial background on a junction flow configuration. Therefore, the investigation relies on the creation of a dedicated test case and an experimental database, which is used to evaluate different types of modelings ranging from one transport equation Reynolds-averaged Navier–Stokes (RANS) turbulence model to large-eddy simulation (LES). The effects of the angle of attack and the boundary-layer thickness are also investigated.

II. Experimental and Numerical Setup

A. Test Case

The investigated test case consists of a wing mounted on a flat plate, as illustrated in Fig. 3. The wing is a NACA0012 of 0.2 m chord. It was selected because of its low BF that sets the test case in a region where the horseshoe vortex and a corner separation could coexist (see Fig. 2). Because of the experimental facilities, the span of the wing was equal to 2.5 c (see the description of the experimental setup in the next section). The Re_c had to be limited to a rather low value to allow LES calculations on this case. Therefore, it was set to $Re_c = 2.8 \times 10^5$ and the incoming boundary-layer thickness was set

Presented at the 40th Fluid Dynamics Conference and Exhibit, Chicago, Illinois, June 28–July 1, 2010; received 29 June 2011; revision received 13 April 2012; accepted for publication 13 April 2012.

*Research Scientist, Applied Aerodynamics Department; fabien.gand@onera.fr.
†Research Scientist, Applied Aerodynamics Department.
‡Research Scientist, Applied Aerodynamics Department.

Fig. 1 Corner separation on the DLR-F6 [1].

to $\delta/T = 0.6$ at $x/c = -0.5$ upstream of the wing. This leads to MDF $= 1 \times 10^8$.

Preliminary studies at various angles of attack lead to setting this parameter at 7 deg to create a significant pressure gradient around the wing (the wing stall occurs around 10 deg at this low Re_c). This set of parameters are referred to as "baseline configuration" in the following. The effect of the angle of attack (increased to 10 deg) and of the boundary-layer thickness (decreased to $\delta/T = 0.3$) are also investigated.

B. Experimental Setup

The measurements presented in the present paper were made in the S2L wind tunnel at ONERA Meudon, France. This open-circuit research facility, depicted in Fig. 4, has a circular test section of 1 m in diameter. Compared to the thickness of the wing (24 mm), this section should be enough to limit side-wall and confinement effects. RANS calculations of the flow with and without the wind-tunnel walls included are presented in the next part to support this assumption (see Sec. III.A).

The pressure distribution around the wing at midspan was measured by static pressure sensors, the incoming boundary layer was probed using a boundary-layer pressure probe, and the mean flow was measured using a five-hole probe 1.5 mm in diameter.

The flat plate was put at the middle height of the test section and the wing was mounted perpendicular to the plate, spanning the whole test section. Hence, the span of the wing corresponded to 2.5 chords. Oil-flow visualizations were carried out to ensure that no major corner separation occurs at the junction between the wing and the wind-tunnel wall. The length of the flat plate upstream of the wing was tuned to recover the targeted boundary-layer thickness at $x/c = -0.5$.

The turbulent boundary layer on the flat plate was triggered by a tripping line at the leading edge of the flat plate made out of carborundum grains of 160 μm in diameter. The same carborundum grains were used to trigger the turbulent transition on the wing. The tripping line was set at $x/c = 5\%$ to avoid the onset of a laminar separation bubble at the leading edge.

C. Numerical Setup

The numerical study involved two major turbulence-modeling approaches. Steady RANS calculations with different turbulent closures were tested, as well as LES.

Because of numerical difficulties at low Mach numbers, the Mach number of the test case was increased from 0.06 to 0.15. However, the value of Re_c was kept at the same value as the experiments by lowering the freestream total pressure for the calculations.

The RANS computations that are presented in the following section were performed using the ***elsA*** software developed at ONERA. The averaged Navier–Stokes equations were solved using a finite volume method on multiblock structured grids. The multigrid technique was used to accelerate the convergence, and time integration was performed using a first-order implicit backward Euler scheme. The second-order-centered scheme of Jameson was used to discretize the Euler fluxes. Low-speed preconditioning was used to avoid numerical difficulties linked to the low Mach number.

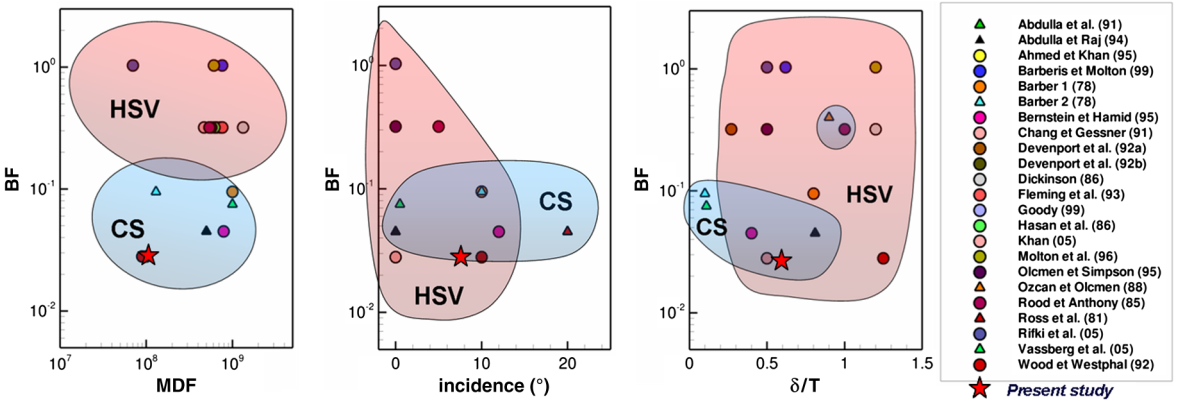

Fig. 2 Flow parameters of the major simplified junction flow studies and dominant flow features observed [circle: massive horseshoe vortex (HSV); triangle: corner separation (CS)]. Data from [7–26].

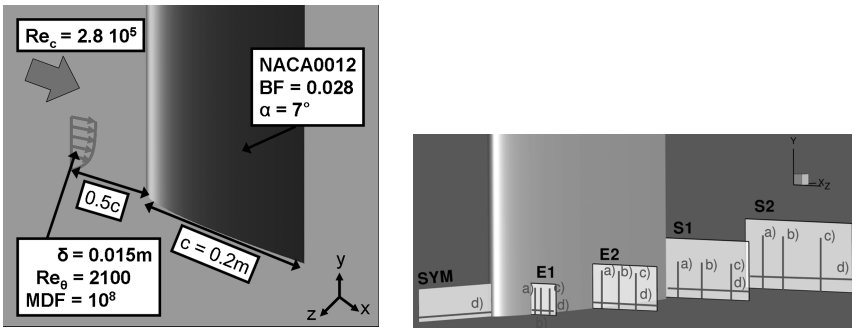

a) Definition of the test case

b) Definition of the planes and rakes used in the study

Fig. 3 Test case investigated.

Fig. 4 Wind-tunnel setup.

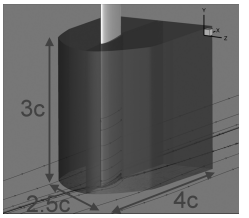

Fig. 5 Grid refinement area.

In this paper, we report the results obtained with the Spalart–Allmaras (SA) [27] model (with and without the rotation correction of Shur et al. [28]), the Wilcox k-ω model [29], the Menter SST k-ω model [30], and the Speziale–Sarkar–Gatski Reynolds stress model in its low-Reynolds-number implementation (RSM) [31]. This choice of turbulent closures is supposed to give a good overview of the capacities of the RANS approach in the framework of junction flows.

The issue of turbulent transition has been investigated by imposing a laminar area at the wing leading edge in the simulation with the SA model to mimic the experimental setup. This computation was compared to a computation where no laminar area had been imposed to investigate the influence of this parameter. The results of the computations revealed insensitivity to the presence of the laminar area, thus all RANS computations were performed in fully-turbulent mode.

For the RANS computations, three grids were used to assess the grid convergence of the results and select the mesh used to investigate the turbulence-modeling effect. The grid convergence study is presented in Sec. III.A.

The LES simulation was performed using the FLU3M code developed by ONERA. Time integration was performed by a second-order accurate backward scheme of Gear, while the spatial integration was carried out by a AUSM + (P) scheme introduced by Mary and Sagaut [32]. Further details concerning the numerical method can be found in Péchier et al. [33]. The selective mixed scales subgrid-scale model of Lenormand et al. [34] was used to model the small scales. The inflow conditions were generated by an adaptation of the original synthetic eddy method of Jarrin et al. [35] proposed by Pamiès et al. [36].

The central processing unit (CPU) cost per cell and per inner iteration was less than 0.3×10^{-6} s. The simulation was performed on eight processors of a NEC-SX8 supercomputer and the code was run at approximately 7×10^9 floating-point operations per second on each processor. The time step was fixed to $\Delta t_{\mathrm{CFD}} = 0.55\ \mu$s, which corresponds to a normalized time-step $\Delta\tilde{t} = \Delta t_{\mathrm{CFD}} \cdot U_e/\delta_0 = 2.5 \times 10^{-3}$. The temporal accuracy of the calculation was checked during the inner-iteration process (six Newton-like inner iterations were used to reach second-order time accuracy). A decrease of the inner residuals of at least one order was obtained. The Courant–Friedrich–Levy number based on the maximum acoustic velocity $(U + a)$ and the minimum cell size [$\mathrm{CFL} = (U + a)\Delta t/\min(\Delta x, \Delta y, \Delta z)$] was lower than 14, which ensured the temporal accuracy of the simulation because an implicit scheme was used.

The grid was generated following the usual LES guidelines for wall turbulence. Spacing in the longitudinal direction is $\Delta x^+ = 50$, $\Delta z^+ = 25$ in the transverse direction and $\Delta y^+ = 1$ in the wall-normal direction. The grid contained 63.10^6 grid points distributed among 53 blocks.

The turbulent transition was triggered by a small step located at 5% c to reproduce the effect of the experimental tripping line. The step had the same thickness as the carborandum grains used during the wind-tunnel tests, i.e., 160 μm. A posteriori analysis of the results showed that the wing boundary layer downstream of the step was actually turbulent, which justified the procedure used to trigger the turbulent transition in the LES computation.

A thorough analysis of the LES calculation and comparison with the experiment, including second-order statistics and spectral properties is given in Gand et al. [5] to provide physical insights on the junction flow. In this paper, only time-averaged results from the LES computation over 70 ms are presented in the framework of the turbulence-modeling investigation.

III. Evaluation of Reynolds-Averaged Navier–Stokes and Large-Eddy Simulation Modelings

A. Preliminary Verifications

Preliminary checks were required to verify the validity of the comparisons between the experimental, RANS, and LES simulations. The effect of the walls of the wind tunnel, the grid dependence of the RANS results, and the experimental and numerical flow conditions are investigated in this section.

It is well known from the literature that the grid used has a critical influence on the result of junction flows simulation [4]. As a consequence, a grid convergence study was performed using three meshes. The first mesh contained 12.10^6 nodes and the first wall cell was located at $y^+ = 1$ both on the flat plate and the wing. In this mesh, a wide area comprising the junction was selected (see Fig. 5). In this area, the grid was coarsened or refined by a factor of 2 in each direction to create a coarse and a fine mesh. The coarse mesh contained 7.10^6 nodes; the first wall cell was then located at $y^+ = 2$ in the junction area. The fine mesh comprised 60.10^6 nodes and had a resolution of $y^+ = 0.5$ at the walls. In the following discussion, the 7.10^6, 12.10^6, 60.10^6 grids are referred to as grids 1, 2, and 3, respectively.

Figure 6 illustrates the results of the grid density investigation for the Spalart–Allmaras model and the RSM model. The contours of total pressure loss $Cpi = (Pi_0 - Pi)/(1/2 \cdot p \cdot U_0^2)$ are plotted, which allows an evaluation of the energy loss associated with the horseshoe vortex core and the corner separation and to compare it with the energy loss generated by an isolated boundary layer.

The flow visualizations provided show the dramatic influence of the grid resolution on the solution given by the RANS models. Actually, both SA and RSM models require at least 12.10^6 grid points to provide a solution on the asymptotic range of convergence. The solutions obtained on mesh 1 are clearly not reliable. The SA model predicts a massive separation at the junction for the coarser mesh, while the separation size decreases and reaches a stable value on mesh 2 and mesh 3. On the other hand, the streamlines indicate that the RSM model fails to properly develop wall turbulence with mesh 1. Nevertheless, the results obtained with mesh 2 and mesh 3 look very similar and agree fairly well with the SA results on the same meshes.

A more accurate evaluation of the grid convergence study is provided in Fig. 7. The grid convergence index (GCI) introduced by Roache [37] is used to assess the level of grid convergence reached. Actually, the GCI was proposed to report grid convergence results in a consistent fashion based on the Richardson approximation. The main idea is to provide the relative error between two solutions, taking into account the ratio of the cell sizes and the order of accuracy of the spatial scheme. Considering two simulations carried out on a coarse mesh of grid spacing h_2 and a fine mesh of grid density $h_1 = h_2/r$, one can approximate the relative error for the variable f

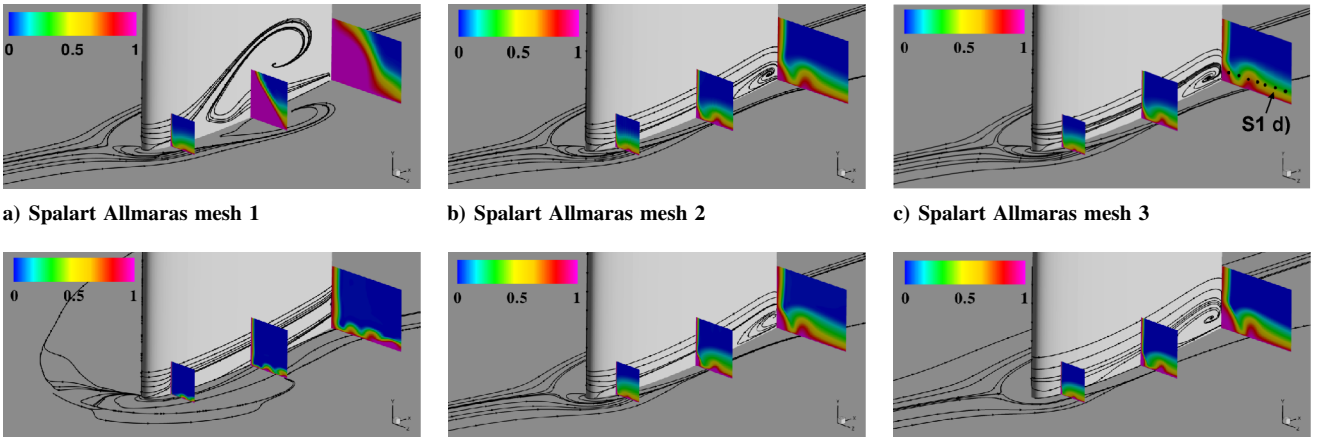

a) Spalart Allmaras mesh 1 b) Spalart Allmaras mesh 2 c) Spalart Allmaras mesh 3

d) RSM mesh 1 e) RSM mesh 2 f) RSM mesh 3

Fig. 6 Flow visualizations of the solutions given by the SA and RSM models on different meshes.

on the coarse mesh h_2 with a pth order accurate scheme by $E_2(f) = \epsilon r^p/(r^p - 1)$, with $\epsilon = |(f_2 - f_1)/f_1|$. The GCI is then defined for the variable f on the mesh h_2 as $\mathrm{GCI}_2(f) = F_s|E_2| = F_s\epsilon r^p/(r^p - 1)$, where F_s is a safety factor taken as being equal to 3 following the recommendation of Roache [37]. In our case, the GCI is computed with the second-order scheme of Jameson, grid 2 as the coarse grid, and grid 3 as the fine grid: $\mathrm{GCI}_2(f) = 4|(f_2 - f_1)/f_1|$. The variable f chosen for the present study is Pi/Pi_0, where Pi_0 is the reference stagnation pressure.

The profiles of Cpi along rakes S1 a) and S1 d) depicted in Fig. 7 show that the solutions on meshes 2 and 3 are very similar (note that the corner separation area is covered by these two rakes). The low values of GCI ensure that the solution on mesh 2 is grid-converged for the SA model. The results for the RSM model tend to indicate that the solution is not completely grid-converged, but the results on grid 2 are on the asymptotic range of convergence. Of interest, it seems that the grid refinement from grid 2 to grid 3 for the RSM model tends to shift the horseshoe vortex slightly away for the wing shown by the displacement of the peak of Cpi characteristic of the vortex core in Fig. 7b. Nevertheless, it appears that the solutions obtained with grid 2 for both models have minimal spatial discretization errors (almost none for the SA model), thus the RANS simulations presented in the rest of the article were performed with this grid.

Once the spatial discretizations are minimized, another common source of uncertainty for the experimental/numerical comparisons is the influence of the wind-tunnel walls. To investigate this matter, the results of a RANS simulation performed with the wind-tunnel walls included or excluded are compared in Fig. 8. Both of these simulations were performed using the Spalart–Allmaras turbulence model, the grid used for the simulation with the walls excluded is grid 2 defined previously. The grid used for the simulations with the walls included has the same grid density as grid 2 in the junction area.

Figure 8 depicts the comparison of the global flow parameters. It appears that the pressure distribution at midspan is slightly impacted by the presence of the walls because the minimum Cp is 10% lower than expected in the case where the walls are taken into account. However, the global pressure distribution at midspan is not affected by the presence of the walls. Conversely, almost no difference is observed regarding the incoming boundary layer, which compares well with the experimental data.

The flow visualizations presented in Fig. 9 are very similar. As a matter of fact, the presence of the walls does not seem to have any influence on the flow simulation nor on the phenomena captured by the RANS simulation. The horseshoe vortex is captured in each case, as well as the corner separation that appears at the trailing edge of the

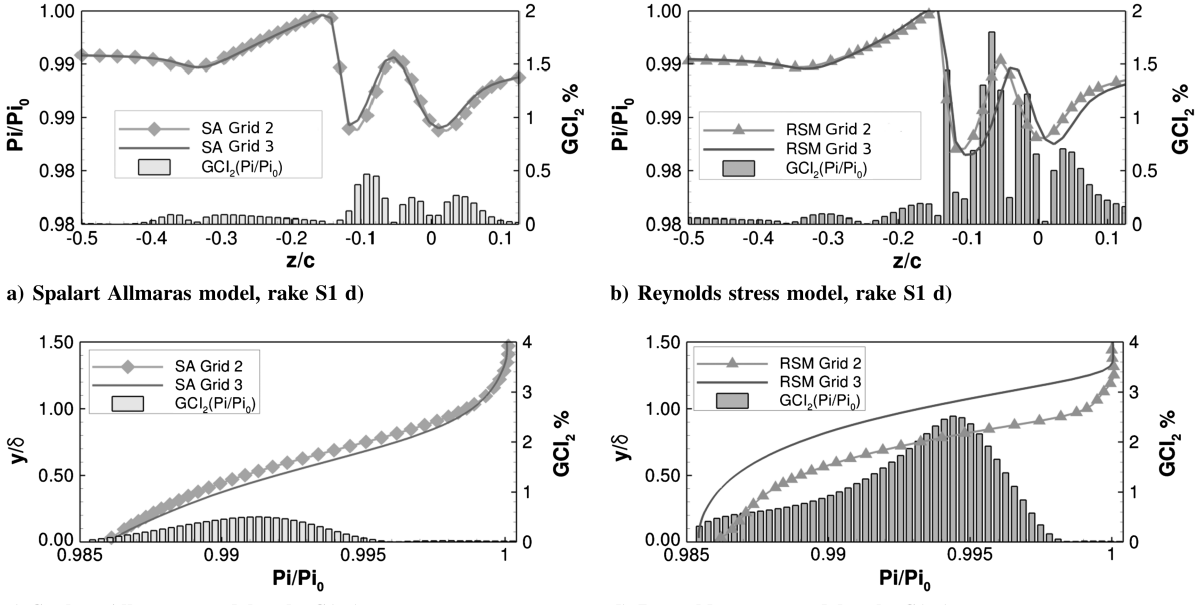

a) Spalart Allmaras model, rake S1 d) b) Reynolds stress model, rake S1 d)

c) Spalart Allmaras model, rake S1 a) d) Reynolds stress model, rake S1 a)

Fig. 7 Quantitative evaluation of the grid convergence for the Spalart–Allmaras and Reynolds stress model models.

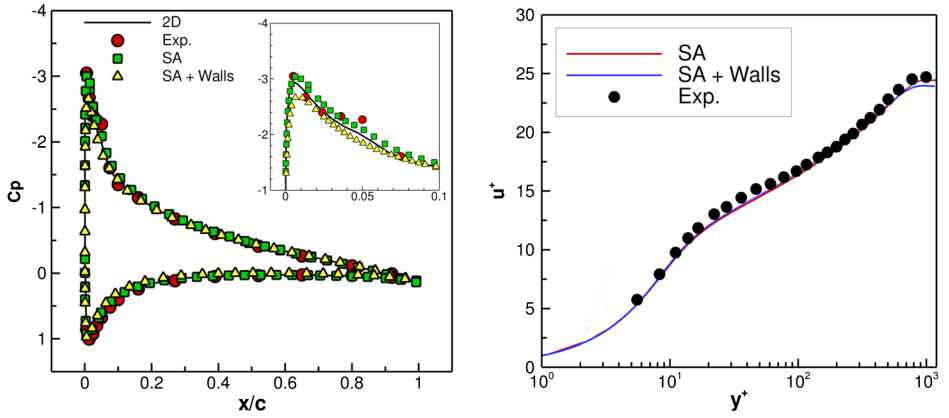

a) Pressure distribution at mid span b) Boundary layer

Fig. 8 Influence of the walls—Flow conditions.

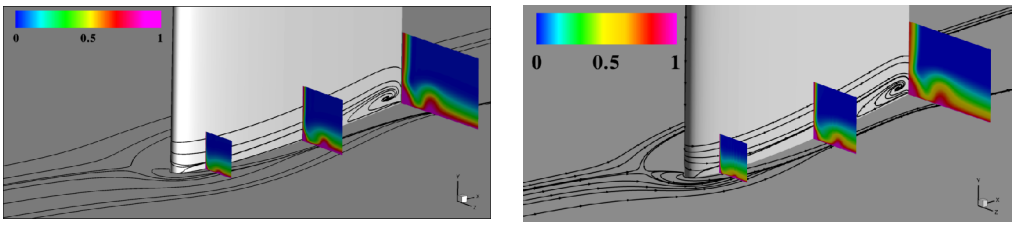

a) Without walls b) With walls

Fig. 9 Influence of the walls—contours of *Cpi*.

wing on the suction side and has the same shape and position for the two simulations.

Figure 10 confirms the qualitative interpretations made previously in this paper. The Cpi profiles plotted show that the effect of the presence of the walls is negligible within the framework of our study. It appears that the horseshoe vortex is slightly shifted away from the wing when the walls are not included. This observation, along with the Cp distributions at midspan, tend to indicate that the effect of the walls could be taken into account with an angle of attack correction because the pressure gradient around the wing is slightly decreased, but there are no major flow modifications due to the presence of the walls. Because the effect of the walls on the simulation is very limited and do not change the main results, one can conclude that the wind-tunnel walls do not create a significant confinement effect. Therefore, in the rest of the paper we only present simulations where the presence of the walls is not taken into account, the implementation of which is more straightforward.

Finally, the aerodynamic conditions need to be carefully monitored to ensure that the experimental and numerical fields are comparable. The experimental, RANS, and LES pressure distribution at midspan are plotted in Fig. 11a. The overall pressure gradient around the wing is fairly well reproduced by the computations, meaning that the angle of attack was correctly set up during the simulations. In the leading edge area on the suction side, a slight stall of the Cp curve is observed in the LES result, which indicates the presence of a laminar separation bubble for $x/c < 10\%$. Downstream of this station, the Cp curve fits fairly well with the experimental data which shows that the boundary layer on the wing has become turbulent in the LES and the correct pressure distribution around the wing is achieved. As mentioned previously, RANS computations with and without taking into account the laminar area at the leading edge have been carried out. These computations showed that the circulation-related effects resulting from the presence of this laminar area were negligible. Therefore, because the

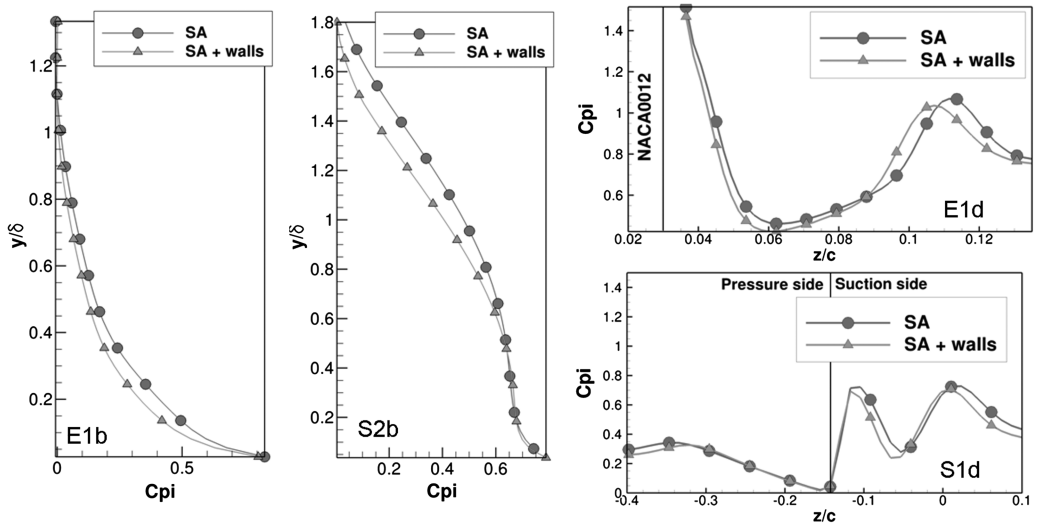

Fig. 10 Influence of the walls—*Cpi* levels on rakes defined in Fig. 3.

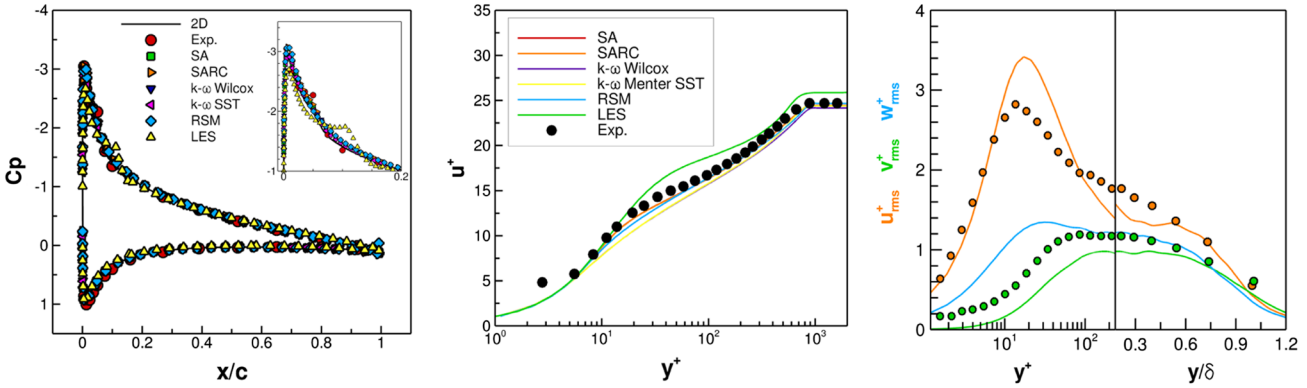

a) Pressure distribution at mid span

b) Incoming boundary layer

c) Mean velocity fluctuations within the LES boundary layer, exp. data from[38] at $Re_\theta = 2900$

Fig. 11 Verification of the aerodynamic conditions of the experiments and computations.

junction flow is mainly driven by the overall pressure gradient around the wing, we consider that this discrepancy between the experimental data and LES in the leading edge area is not significant within the framework of the present study.

The properties of the incoming boundary layer (defined at $x/c = -0.5$ upstream of the nose of the wing) are investigated in Figs. 11b and 11c. The mean velocity profiles shown in Fig. 11b indicate that the thickness and friction coefficient of the boundary layers computed with the RANS models are in very good agreement with the experimental measurements. The slope of the logarithmic region of the boundary-layer profile, as well as the friction coefficient, are not correctly reproduced by the LES. This is a common limitation of this kind of approach when used with finite volume, second-order schemes. Besides, the distribution of the velocity fluctuations within the incoming boundary layer is fairy well reproduced, as depicted in Fig. 11c, in which the validation data were taken from De Graaf and Eaton experiments [38] at a slightly higher Re_θ because the present experimental setup did not allow that kind of measurement. The results obtained for the second-order statistics are typical of LES simulations of wall turbulence performed with second-order schemes found in references [36,39].

As the preliminary studies presented in this section have shown, the numerical simulations have reproduced the aerodynamic conditions of the wind-tunnel tests and are representative of the best results achievable with the RANS models tested in this study (as justified by the grid convergence study) and with the LES approach with second-order schemes. Therefore, the next section focuses on the comparison of the experimental and numerical data within the junction flow.

B. Effect of the Turbulence-Modeling on the Baseline Configuration

The comparison of the experimental, RANS, and LES flowfields in Fig. 12 illustrates the issues at stake in the present study. Two points are addressed in the following paragraphs: the issue of the corner separation predicted by the RANS model but that does not exists in the wind-tunnel measurements, and the behavior of the time-averaged horseshoe vortex. Both help understand the assets and limitations of the numerical approaches investigated.

In the first place, it appears that the experimental measurements do not show any evidence of a corner separation on the aft part of the junction. If there was any separation, it would be easily visible in the Cpi contours as it is for the RSM results, which are therefore inaccurate. Conversely, the LES flowfield depicted in Fig. 12b appears to agree fairly well with the experimental flow in the corner area. This is confirmed by the plot of Cpi close to the junction in Fig. 12d, in which the limitations of the RANS models used in this study are dramatically illustrated. While every RANS result presents a plateau of total pressure loss characteristic of a separation in the corner, the experimental and LES curves are typical of the evolution of the total pressure losses within an attached boundary layer.

In a previous study [5] of the present test case, which aimed at investigating the unsteady physics of this junction flow, the high level of turbulence anisotropy in the neighbourhood of the junction has been identified. As a consequence, it is not surprising that the first order RANS models that rely on the Boussinesq approximation are not able to simulate such a complex flow. Second-order turbulent closures such as the RSM model used in this study are theoretically able to reproduce anisotropic turbulence because they compute the Reynolds stresses directly. However, the results presented in Fig. 12 show that even this advanced turbulent closure fails to reproduce the main flow features observed experimentally.

To investigate the behavior of the RSM model, it is useful to use the formalism introduced by Lumley and Newman [40] to quantify the level of anisotropy. Anisotropy maps involve the second and third invariants II_b and III_b of the anisotropy tensor $b_{ij} = \frac{\overline{u_i u_j}}{u_s u_s} - \frac{1}{3}\delta_{ij}$. Lumley and Newman showed that all realizable states of turbulence are bounded within a triangle which is defined by the limiting states of turbulence in the (II_b, III_b) frame. Basically, the bottom of the triangle corresponds to isotropic turbulence and the higher corner represents one-component turbulence. An anisotropy map extracted from the LES and RSM results close to the corner is presented in Fig. 13. This plot show that the model seems unable to reproduce the maximum anisotropy reached in LES, which could explain the discrepancies observed between RANS and experimental and LES results. This also suggest an important correlation between the anisotropy of the corner flow and the onset of corner separations, but the data presented here are too sparse to investigate this issue further as it is beyond the scope of this paper.

In addition to the failure to reproduce high levels of anisotropy, it is important to note that the limitations of the RANS approach for such junction flow may also come from the overall unsteadiness of the horseshoe vortex [5], which plays an important part in the interaction between the horseshoe vortex and the corner separation onset.

The evolution of the time-averaged horseshoe vortex can be scrutinized using the flow visualizations presented in Figs. 12a–12c. The print of the suction-side horseshoe vortex is identified easily on the experimental contours of total pressure losses, the vortex is drowned into the flat plate boundary layer. The same trend is observed in the RSM contours, while the horseshoe vortex appears weaker and more dissipated in the wake in the LES contours shown in Fig. 12b.

The plots of Figs. 12e–12h provide a quantitative assessment of the accuracy of each approach in the horseshoe vortex convection area. It appears that the maximum levels of total pressure losses, indicating the location of the horseshoe vortex core, are overestimated by the RANS models by 10–25% depending on the station and the model. On the other hand, these levels are underestimated by the LES by 10%, which denotes the premature diffusion of the horseshoe vortex in the LES. Acknowledging that the values of the ratio of the subgrid-scale viscosity to the freestream viscosity in the junction area remains lower than 3, this excessive diffusion by the LES is attributed to the dissipation of the second-order numerical schemes.

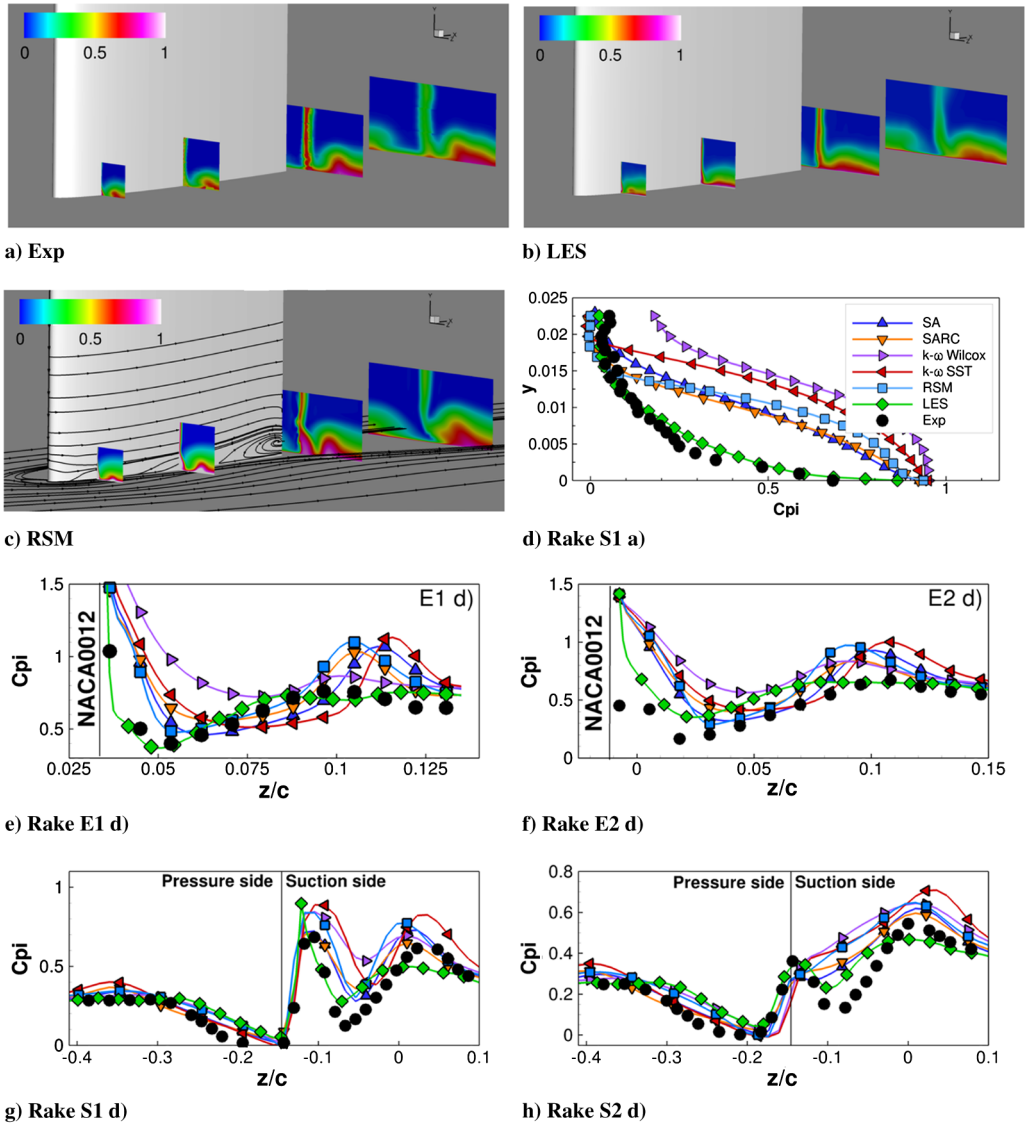

Fig. 12 Influence of the turbulent closure—contours and plots of *Cpi* along the junction and near the corner. The rakes are defined in Fig. 3.

C. Sensitivity Study

In the previous section, it was shown that RANS calculations do not provide an accurate representation of the flow around the baseline configuration. Nevertheless, from an industrial point of view, it is interesting to wonder whether the sensitivities of the baseline configuration to changes in aerodynamic conditions can be reproduced by these models and to which extent, because they are the only computational methods affordable at design stages.

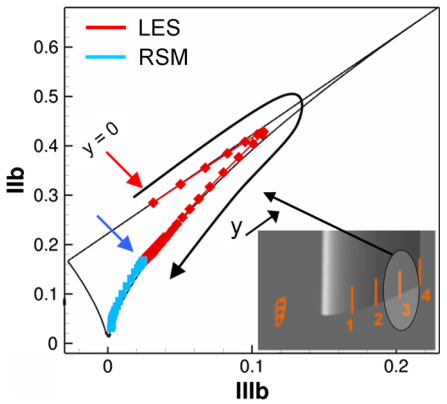

Fig. 13 Evolution of the anisotropy map along the corner. Red: LES; Blue: RSM.

The influence of the angle of attack is investigated in Fig. 14. Flow visualizations of the baseline configuration at 7 and 10 deg are presented.

Figures 14a and 14b depict the evolution of the horseshoe vortex observed during the experiments: the vortex at the suction side is pushed away from the wing by the pressure distribution, which is confirmed by the experimental plots of Cpi in rake S1 d) (see Fig. 3 for the definition of the rake) in Fig. 14c. This behavior is in agreement with the previous observations of Arnott and Bernstein [41].

Nevertheless, one can see in Fig. 14b that the Cpi values at the two first stations for the 10 deg case are somewhat lower than those of the 7 deg case at the same locations, which seems to indicate a weaker vortex. This is supposed to be caused by the shifting of the vortex away from the wing beyond the measurement planes. Besides, the values of Cpi downstream of these stations show that the horseshoe vortex is actually stronger in the 10 deg case.

Apart from the change of position of the horseshoe vortex, no significant difference is visible between the two configurations measured experimentally. In particular, no corner separation is onset by the increase of the angle of attack, while the wing is close to stall at 10 deg. This means that the transition to stall does not involve the growth of a corner separation and extension of the separated area to the whole wing. This is to be linked to the 2-D behavior of the NACA0012 airfoil, for which the stall separation starts from the leading edge for this range of Re_c, whereas for thicker airfoils it starts

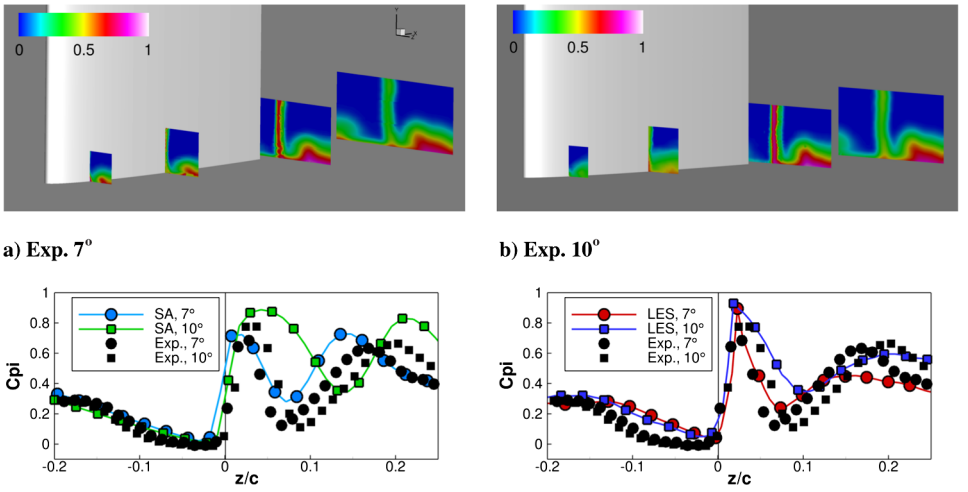

a) Exp. 7° b) Exp. 10°

c) Rake S1 d), exp. vs SA results d) Rake S1 d), exp. vs LES results

Fig. 14 Influence of the angle of attack. The rakes are defined in Fig. 3.

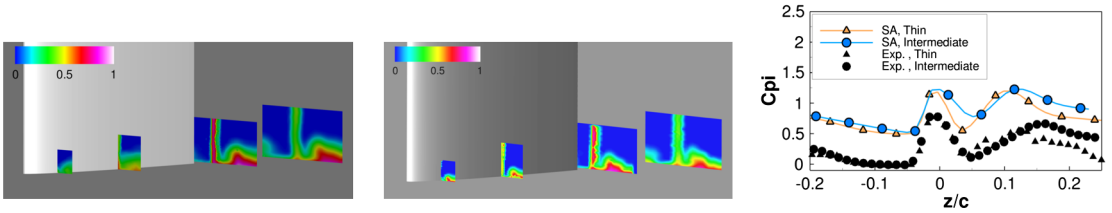

a) exp., $\delta_{x/c\ =-\ 0.5}$ = 0 .015m b) exp., $\delta_{x/c\ =-\ 0.5}$ = 0 .007m c) Rake S1 d) exp. vs SA (exp. levels offset by 0.5)

Fig. 15 Influence of the incoming boundary layer.

from the trailing edge. Therefore, we assume that the design of the wing prevents the onset of a corner separation on this configuration because the stall occurs suddenly.

On the numerical side, Figs. 14c and 14d indicate that both RANS and LES are able to capture the effect of the angle of attack increase. As a matter of fact, one can see that the maximum of the Cpi curves is shifted towards higher values of z/c in every case, as expected from the experimental data.

Figure 15 depicts the sensitivity of the baseline configuration to the thickness of the incoming boundary layer. No major evolution is observed on the experimental visualizations. One can still note that the horseshoe vortex is smaller in the thin boundary-layer case. This was expected because the MDF for the thin boundary-layer case is lower than that of the thick boundary-layer case. Furthermore, the horseshoe vortex is closer to the flat plate in the thin boundary-layer case.

The change of position and strength of the horseshoe vortex is quite well predicted by the RANS simulation (no LES data are available for this case due to the CPU cost of such simulations), even if a spurious corner separation is still present in the calculations, as illustrated by the shape of the peak of Cpi near $z/c = 0$ on the blue curve in Fig. 15c.

IV. Conclusions

In this study, Reynolds-averaged Navier–Stokes (RANS) models and large-eddy simulations (LES) were used to simulate a simplified wing-body junction flow consisting of a NACA0012 wing mounted on a flat plate at $Re_c = 2.810^5$ and an angle of attack of 7 deg. Wind-tunnel test were carried out to provide reference data for the simulations.

The results have emphasized the limitations of the RANS models selected for the present study for this type of flow. Actually, the RANS simulations predicted a corner separation that was not observed during the experiments. Conversely, LES simulations were in good agreement with the wind-tunnel data.

The failure of RANS models to reproduce the flow observed experimentally has been attributed to the high level of anisotropy in the junction that cannot be reproduced by first-order models and that is underestimated with the second-order model tested. The complex unsteady behavior of the horseshoe vortex is also a major difficulty for the statistical models.

The discrepancies observed between the LES simulation and the wind-tunnel data, namely the dissipation of the horseshoe vortex in the wake, are attributed to the accuracy of the second-order numerical schemes.

A sensitivity study was performed to evaluate the influence of the pressure gradient around the junction and of the thickness of the incoming boundary layer. It was shown that no corner separation is triggered by an increased pressure gradient around the junction, which leads to the thought that the intrinsic properties of the NACA0012 airfoil prevents the onset of a corner separation due to its tendency to suddenly stall from the leading edge. Numerical results tend to show that even if RANS results (obtained with the Spalart–Allmaras model) are erroneous in their absolute value, the sensitivities of the flow can be predicted to some extent using the statistical approach.

Future work will be devoted to the design and analysis of another wing-body junction flow test case, which should present a corner separation to investigate this flow feature that remains poorly understood and yet problematic for aircraft makers. A better understanding of the corner separation and the mechanisms leading to it should also help improve the second-order closures to provide reliable RANS models for design stages.

Acknowledgments

The authors would like to thank Vincent Brion, Michel Alaphilippe, Nicolas Severac, Jean François Pulizzi, Philippe Huet,

and François Lambert from the experimental department at ONERA for their invaluable help during the wind-tunnel tests.

References

[1] Tinoco, E. N., Venkatakrishnan, V., Winkler, C., Mani, M., Vassberg, J., and Kulfan, B. M., "Structured and Unstructured Navier-Stokes Solvers for the Third Drag Prediction Workshop," *Journal of Aircraft*, Vol. 45, No. 3, 2008, pp. 738–749. doi:10.2514/1.30593

[2] Murayama, M., Imamura, T., and Yamamoto, K., "Comparison of RANS Simulations of Multi-Element High-Lift Configurations," AIAA Paper 2006-1396, Jan. 2006.

[3] Li, C., Ye, Z., and Wang, G., "Simulation of Flow Separation at the Wing Body Junction with Different Fairings," *Journal of Aircraft*, Vol. 45, No. 1, 2008, pp. 258–266. doi:10.2514/1.26638

[4] Simpson, R., "Junction Flows," *Annual Review of Fluid Mechanics*, Vol. 33, No. 1, 2001, pp. 415. doi:10.1146/annurev.fluid.33.1.415

[5] Gand, F., Deck, S., Brunet, V., and Sagaut, P., "Flow Dynamics Past a Simplified Wing Body Junction," *Physics of Fluids*, Vol. 22, No. 11, Nov. 2010, pp. 115111–115116. doi:10.1063/1.3500697

[6] Fleming, J., Simpson, R., and Devenport, W., "An Experimental Study of a Turbulent Wing-Body Junction and Wake Flow," Aerospace and Ocean Engineering Department, Virginia Polytechnic Inst. and State Univ., Technical Report VPI-AOE-179, Blacksburg, VA, 1991.

[7] Fleming, J., Simpson, R., Cowling, J., and Devenport, W., "An Experimental Study of a Turbulent Wing-Body Junction and Wake Flow," *Experiments in Fluids*, Vol. 14, No. 5, 1993, pp. 366–378. doi:10.1007/BF00189496

[8] Abdulla, A., Bhargava, R., and Raj, R., "An Experimental Study of Local Wall Shear Stress, Surface Static Pressure, and Flow Visualization Upstream, Alongside, and Downstream of a Blade Endwall Corner," *Journal of Turbomachinery*, Vol. 113, No. 4, 1991, pp. 626–632. doi:10.1115/1.2929128

[9] Abdulla, A., and Raj, R., "Three Dimensional Flow Structure in the Wake of a Wing Body Juncture," AIAA Paper 1994-2289, June 1994.

[10] Ahmed, A., and Khan, M., "Effect of Sweep on Wing Body Juncture Flows," AIAA Paper 1995-0868, Jan. 1995.

[11] Barberis, D., and Molton, P., "Shock Wave—Turbulent Boundary Layer Interaction in a Three Dimensional Flow," AIAA Paper 1995-0227, Jan. 1995.

[12] Barber, T., "An Investigation of Strut-Wall Intersection Losses," *Journal of Aircraft*, Vol. 15, No. 10, 1978, pp. 676–681. doi:10.2514/3.58427

[13] Bernstein, L., and Hamid, S., "On the Effect of a Swept Wing Plate Junction Flow on the Lift and Drag," *The Aeronautical Journal*, Vol. 99, No. 987, 1995, pp. 293–305.

[14] Chang, B., and Gessner, F., "Experimental Investigation of Flow About a Strut-Endwall Configuration," *AIAA Journal*, Vol. 29, No. 12, 1991, pp. 2105–2114. doi:10.2514/3.10847

[15] Devenport, W., and Simpson, R., "Flow Past a Wing Body Junction: Experimental Evaluation of Turbulence Models," *AIAA Journal*, Vol. 30, No. 4, 1992, pp. 873–881. doi:10.2514/3.11004

[16] Devenport, W., Agarwal, N., Dewitz, M., and Simpson, R., "Effects of a Leading Edge Fillet on the Flow Near and Past an Appendage Body Junction," *AIAA Journal*, Vol. 30, No. 9, 1992, pp. 2177–2183. doi:10.2514/3.11201

[17] Dickinson, S., "An Experimental Investigation of Appendage-Flat Plate Junction Flow, Vol. 1: Description," Naval Ship Research and Development Center, Technical Report DTNSRDC-86/051, Bethesda, MD, 1986.

[18] Goody, M., "An Experimental Investigation of Pressure Fluctuations in Three Dimensional Turbulent Boundary Layers," Ph.D. Thesis, Virginia Polytechnic Inst. and State Univ., Blacksburg, VA, 1999.

[19] Hasan, M., Casarella, M., and Rood, E., "An Experimental Study of the Flow and Wall Pressure Field Around a Wing-Body Junction," *Journal of Vibration, Acoustics, Stress, and Reliability in Design*, Vol. 108, No. 3, 1986, pp. 308–314. doi:10.1115/1.3269344

[20] Khan, J., "Topological Model of Flow Regimes In The Plane of Symmetry of a Surface Mounted Obstacle," *Physics of Fluids*, Vol. 17, No. 4, 2005, p. 045101. doi:10.1063/1.1864072

[21] Olçmen, S., and Simpson, R., "An Experimental Study of a Three-Dimensional Pressure Driven Turbulent Boundary Layer," *Journal of Fluid Mechanics*, Vol. 290, May 2005, pp. 225–262. doi:10.1017/S0022112095002497

[22] Rood, E., and Anthony, D., "Tail Profile Effects on Unsteady Large Scale Flow Structure in the Wing and Plate Junction," *Forum on Unsteady Flow*, American Society of Mechanical Engineers, Paper FGD 27, New York, 1985.

[23] Ross, J., Vogel, J., and Corsiglia, V., "Full-Scale Wind Tunnel Study of Wing Fuselage Interaction and Comparison with Paneling Method," AIAA Paper 1981-1666, Aug. 1981.

[24] Rifki, R., Khan, J., Ahmed, A., and Bangash, Z., "Effect of the Aspect Ratio on the Flow Field on Surface Mounted Obstacles," AIAA Paper 2005-4848, June 2005.

[25] Vassberg, J., Sclafani, A., and DeHaan, M., "A Wing-Body Fairing Design for the DLR-F6 Model: a DPW-III Case Study," AIAA Paper 2005-4730, June 2005.

[26] Wood, D., and Westphal, R., "Measurements of the Flow Around a Lifting Wing/Body Junction," *AIAA Journal*, Vol. 30, No. 1, 1992, pp. 6–12. doi:10.2514/3.10875

[27] Spalart, P., and Allmaras, S., "A One-Equation Turbulence Model for Aerodynamic Flows," *30th Aerospace Sciences Meeting and Exhibit*, AIAA Paper AIAA-92-0439, Reno, NV, Jan. 6–9, 1992.

[28] Shur, M. L., Strelets, M. K., Travin, A. K., and Spalart, P. R., "Turbulence Modeling in Rotating and Curved Channels: Assessing the Spalart-Shur Correction," *AIAA Journal*, Vol. 38, No. 5, 2000, pp. 784–792. doi:10.2514/2.1058

[29] Wilcox, D., "Reassessment of the Scale-Determining Equation for Advanced Turbulence Models," *AIAA Journal*, Vol. 26, No. 11, 1988, pp. 1299–1310. doi:10.2514/3.10041

[30] Menter, F. R., "Zonal Two Equation (k-ω) Turbulence Models for Aerodynamic Flows," AIAA Paper 1993-2906, July 1993.

[31] Speziale, C., Sarkar, S., and Gatski, T., "Modeling the Pressure-strain Correlation of Turbulence: an Invariant Dynamical Systems Approach," *Journal of Fluid Mechanics*, Vol. 227, June 1991, pp. 245–272. doi:10.1017/S0022112091000101

[32] Mary, I., and Sagaut, P., "Large Eddy Simulation of Flow Around an Airfoil Near Stall," *AIAA Journal*, Vol. 40, No. 6, 2002, pp. 1139–1145. doi:10.2514/2.1763

[33] Péchier, M., Guillen, P., and Caysac, R., "Magnus Effect Over Finned Projectiles," *AIAA Journal of Spacecraft and Rockets*, Vol. 38, No. 4, 2001, pp. 542–549. doi:10.2514/2.3714

[34] Lenormand, E., Sagaut, P., Ta Phuoc, L., and Comte, P., "Subgrid-Scale Models for Large-Eddy Simulations of Compressible Wall Bounded Flows," *AIAA Journal*, Vol. 38, No. 8, 2000, pp. 1340–1350. doi:10.2514/2.1133

[35] Jarrin, N., Benhamadouche, S., Laurence, D., and Prosser, R., "A Synthetic-Eddy-Method for Generating Inflow Conditions for Large-Eddy Simulations," *International Journal of Heat and Fluid Flow*, Vol. 27, No. 4, 2006, pp. 585–593. doi:10.1016/j.ijheatfluidflow.2006.02.006

[36] Pamiès, M., Weiss, P.-E., Garnier, E., Deck, S., and Sagaut, P., "Generation of Synthetic Turbulent Inflow Data for Large Eddy Simulation of Spatially Evolving Wall-Bounded Flows," *Physics of Fluids*, Vol. 21, No. 4, 2009, pp. 045103–045115. doi:10.1063/1.3103881

[37] Roache, P., "Verification of Codes and Calculations," *AIAA Journal*, Vol. 36, No. 5, 1998, pp. 696–702. doi:10.2514/2.457

[38] De Graaff, D., and Eaton, J., "Reynolds Number Scaling of the Flat Plate Turbulent Boundary Layer," *Journal of Fluid Mechanics*, Vol. 422, 2000, pp. 319–346. doi:10.1017/S0022112000001713

[39] Sagaut, P., Deck, S., and Terracol, M., *Multiscale and Multiresolution Approaches in Turbulence*, Imperial College Press, London, 2006.

[40] Lumley, J., and Newman, G., "The Return to Isotropy of Homogeneous Turbulence," *Journal of Fluid Mechanics*, Vol. 82, No. 1, 1977, pp. 161–178. doi:10.1017/S0022112077000585

[41] Arnott, A., and Bernstein, L., "The Aerodynamic Interaction at the Junction between a Forward Swept Wing and a Plate," *The Aeronautical Journal*, Vol. 104, No. 1032, 2000, pp. 67–88.

M. Visbal
Associate Editor